

Article

# Study on the Photocathodic Protection of Q235 Steel by CdIn<sub>2</sub>S<sub>4</sub> Sensitized TiO<sub>2</sub> Composite in Splash Zone

Zheng Ma <sup>1,2,3,4</sup> , Xiumin Ma <sup>2,3,4,\*</sup>, Xiutong Wang <sup>2,3</sup> , Nazhen Liu <sup>2,3</sup>, Xuehui Liu <sup>1</sup> and Baorong Hou <sup>1,2,3,4,\*</sup>

<sup>1</sup> Institute of Marine Science and Technology, Shandong University, No. 72 Binhai Road, Qingdao 266237, China; mazheng1993@yeah.net (Z.M.); xhliu68@126.com (X.L.)

<sup>2</sup> Institute of Oceanology, Chinese Academy of Sciences, No. 7 Nanhai Road, Qingdao 266071, China; wangxiutong@qdio.ac.cn (X.W.); nazhenliu@163.com (N.L.)

<sup>3</sup> Open Studio for Marine Corrosion and Protection, Pilot National Laboratory for Marine Science and Technology, No. 1 Wenhai Road, Qingdao 266200, China

<sup>4</sup> Center for Ocean Mega-Science, Chinese Academy of Sciences, 7 Nanhai Road, Qingdao 266071, China

\* Correspondence: xma@qdio.ac.cn (X.M.); houbr@qdio.ac.cn (B.H.)

Received: 12 November 2019; Accepted: 11 December 2019; Published: 14 December 2019



**Abstract:** In this work, the photo-catalytic activity of TiO<sub>2</sub> is considerably enhanced via sensitization with CdIn<sub>2</sub>S<sub>4</sub>, and its application for protecting Q235 from corrosion in splash zones is examined. TiO<sub>2</sub> nanotube arrays (NTAs) are prepared on a flat Ti substrate via two-step anodization. CdIn<sub>2</sub>S<sub>4</sub> is deposited on the surface of TiO<sub>2</sub> NTAs by hydrothermal reaction. TiO<sub>2</sub> NTAs with enormous specific surface areas and large-diameter hollow nanostructures are found to benefit the immobilization of CdIn<sub>2</sub>S<sub>4</sub>. As a narrow band gap semiconductor, CdIn<sub>2</sub>S<sub>4</sub> is able to extend the light absorption range of TiO<sub>2</sub>, and the construction of an n-n type hetero-junction accelerates the separation of carriers. Strong solar light, which accelerates the corrosion of Q235 in the splash zone area, is converted into the necessary condition for protecting Q235 from corrosion. In this work, TiO<sub>2</sub> is sensitized with MoS<sub>2</sub> microspheres (MoS<sub>2</sub>/TiO<sub>2</sub> nanocomposites), which were prepared on a flat Ti substrate via a two-step anodization and hydrothermal method, sequentially.

**Keywords:** corrosion; photocathodic protection; visible light; narrow bandgap semiconductor; TiO<sub>2</sub>

## 1. Introduction

With the increasing development and utilization of marine resources, metallic materials have been extensively used in ports, cross-sea bridges, and offshore oil platforms over the past decades [1]. As low-carbon steel, Q235 steel (with a yield strength of 235 MP) displays ultra-high cost performance and well strength, and is low-cost, which makes it suitable for bridges, platforms, and other engineering structures [2–4]. However, corrosion poses a challenge to the application of Q235 in the marine environment. Marine corrosion areas are generally divided into mud, immersion, tidal, splash, and atmospheric zones [5–9]. Among these areas, the splash zone experiences the most serious level of marine corrosion due to its alternating dry and wet seasons, abundant amount of sunshine, high salt concentration, and other factors [10–12]. In particular, the corrosion rate of carbon steel could be increased by the corrosion product, which contains a p-type semiconductor, under strong solar light. Specifically, the corrosion rate in the splash zone is approximately 3 to 10 times higher than that recorded in other marine corrosion areas. Therefore, the protection of steel in the splash zone must be examined.

Photocathodic protection, as a new cathodic protection method, has been widely examined by scholars due to its lack of power and anode material consumption and theoretically permanent validity [13–16]. Photocathodic protection is based on the transfer of photo-induced electrons from semiconductors to the surface of the protected metal under light to replace the loss of electrons in the metal. The requirements for effective photocathodic protection are that (1) the semiconductor should be n-type, (2) the semiconductor should possess high photo-induced carrier separation efficiency, and (3) the semiconductor should have a more negative Fermi level than the self-corrosive potential of the protected metal. The performance of photocathodic protection can be improved by sufficient solar light. Hence, this approach is particularly effective for corrosion protection in splash zones with an abundant amount of solar light.

TiO<sub>2</sub> is the most important semiconductor in this area [17,18]. TiO<sub>2</sub> has been widely used in photocracking water and photodegrading organic pollutants and solar cells due to its excellent photoelectric properties and costly performance [19–21]. As a 1D semiconductor material, TiO<sub>2</sub> nanotube arrays (NTAs) have been extensively utilized in photocathodic protection due to their excellent electronic transmission properties [22,23]. However, TiO<sub>2</sub> also demonstrates some defects. For example, the large band gap of TiO<sub>2</sub> can limit its absorption of ultraviolet light below 380 nm, and its high carrier recombination rate leads to a low photon-to-electron conversion efficiency. In addition, the conduction band of TiO<sub>2</sub> is insufficiently negative for Q235. Consequently, electrons from Q235 can be transferred to TiO<sub>2</sub> to accelerate the corrosion. A strategy has been proposed to improve the light absorption of TiO<sub>2</sub>, accelerate the separation of photo-induced carriers, and make the Fermi level negative. Loading a narrow band semiconductor with a negative conductance band on the surface of TiO<sub>2</sub> NTAs and constructing heterojunction simultaneously could be an effective method.

As a narrow band gap (2.1 eV) semiconductor material, CdIn<sub>2</sub>S<sub>4</sub> is an ideal material for improving the visible light response of semiconductor composites [24–29]. The conduction band (−0.76 eV) of CdIn<sub>2</sub>S<sub>4</sub> is more negative than that of TiO<sub>2</sub> (−0.29 V versus NHE), which could cause the negative shift of the Fermi level of TiO<sub>2</sub>. As a ternary semiconductor, CdIn<sub>2</sub>S<sub>4</sub> is much more stable due to the presence of In<sup>3+</sup> along with Cd<sup>2+</sup> [27,30]. It effectively avoids the occurrence of photo-corrosion due to photo-induced holes and •OH in CdS-based systems. In addition, similarly to TiO<sub>2</sub>, CdIn<sub>2</sub>S<sub>4</sub> is an n-type semiconductor. The recombination of photo-induced carriers could be inhibited due to the construction of an n-n heterogeneous type when CdIn<sub>2</sub>S<sub>4</sub> is coupled with TiO<sub>2</sub>. Hence, the proposed loading of CdIn<sub>2</sub>S<sub>4</sub> on the surface of TiO<sub>2</sub> may improve the photoelectrochemical properties of TiO<sub>2</sub>, and Q235 could be protected by this composite via photocathodic protection. Na<sub>2</sub>S/Na<sub>2</sub>SO<sub>3</sub> would be used as hole trapping agents which could rapidly absorb photo-induced holes and •OH on the surface of the composite. The hole trapping agents could further prevent the occurrence of photo-corrosion. By contrast, the alkaline environment provided by Na<sub>2</sub>S/Na<sub>2</sub>SO<sub>3</sub> could negatively shift the Fermi level of the synthetic materials, which is good for the protection of Q235.

In this paper, photocatalytic active CdIn<sub>2</sub>S<sub>4</sub>/TiO<sub>2</sub> NTAs are successfully prepared by using the two-step anodization process and facile hydrothermal method. The photocathodic protection of CdIn<sub>2</sub>S<sub>4</sub>/TiO<sub>2</sub> NTAs for Q235 is examined. XRD, SEM, X-ray photoelectron spectroscopy (XPS), and TEM are used to confirm the success of material preparation. UV-VIS diffuse reflectance and photoluminescence spectra analyses are conducted to characterize the samples. Photochemical experiments are used to investigate the photocathodic protection properties of Q235.

## 2. Results and Discussion

A two-step anodization process was performed to prepare TiO<sub>2</sub> NTAs with large tube diameters. A facile hydrothermal method was also used to load CdIn<sub>2</sub>S<sub>4</sub> nanoparticles on the surface of TiO<sub>2</sub> NTAs.

## 2.1. Results Analysis

### 2.1.1. XRD Analysis

As shown in Figure 1, all diffraction peaks of the standard card (ICDD 00-027-0060) can be found in the curve of pure  $\text{CdIn}_2\text{S}_4$ , and the intensity matches well. This finding indicates the preparation of highly crystalline and pure  $\text{CdIn}_2\text{S}_4$ . For the pristine  $\text{TiO}_2$  NTAs, the main peaks appeared at  $25.4^\circ$ ,  $37.0^\circ$ ,  $37.8^\circ$ ,  $48.1^\circ$ ,  $53.9^\circ$ ,  $55.2^\circ$ ,  $70.5^\circ$ , and  $76.2^\circ$ ; these can be assigned to the (101), (103), (004), (200), (105), (211), (220), and (301) crystalline planes of the anatase structure, respectively (ICDD 01-89-4921). The diffraction peak of Ti (ICDD 01-089-3725) is stronger and sharper than that of  $\text{TiO}_2$ , suggesting that  $\text{TiO}_2$  forms only a thin layer on the Ti sheet. Simultaneously, the weak peaks of the monomer are found in the curve of the synthetic  $\text{CdIn}_2\text{S}_4/\text{TiO}_2$  NTA composites. This finding indicates that a small amount of  $\text{CdIn}_2\text{S}_4$  particles had been successfully loaded onto the surface of the  $\text{TiO}_2$  NTAs.

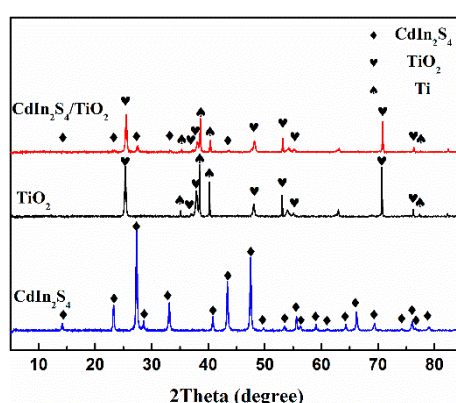


**Figure 1.** XRD patterns of the pure  $\text{TiO}_2$  nanotube array (NTA),  $\text{CdIn}_2\text{S}_4$ , and  $\text{CdIn}_2\text{S}_4/\text{TiO}_2$  NTA composites.

### 2.1.2. SEM Analysis

A morphology image of the prepared  $\text{TiO}_2$  NTAs is shown in Figure 2a. The internal diameter of the tubes was approximately 150 nm, and their wall thickness was 2 nm. These factors could lead to a large load of  $\text{CdIn}_2\text{S}_4$  due to the appearance of load on the surface of the NTAs and the wall of tubes. This finding is due to the relatively large internal diameter, which facilitates the entry of the solution into the tubes. As shown in Figure 2b, the length of  $\text{TiO}_2$  NTAs was found to be  $3.9 \mu\text{m}$ , and independent and ordered tubes were observed. Figure 2c shows the SEM image of the resultant  $\text{CdIn}_2\text{S}_4$ , which was supported on  $\text{TiO}_2$  NTAs. The synthetic  $\text{CdIn}_2\text{S}_4$  shows a relatively symmetrical octahedral or truncated octahedral shape with a smooth surface, grain boundaries, and tip cones. The presence of  $\text{CdIn}_2\text{S}_4$  on the surface and inner part of  $\text{TiO}_2$  NTAs indicates the successful entry of the electrolyte into the tubes. As shown in Figure 2d, the octahedral structure inside the tubes could also be observed in sections.

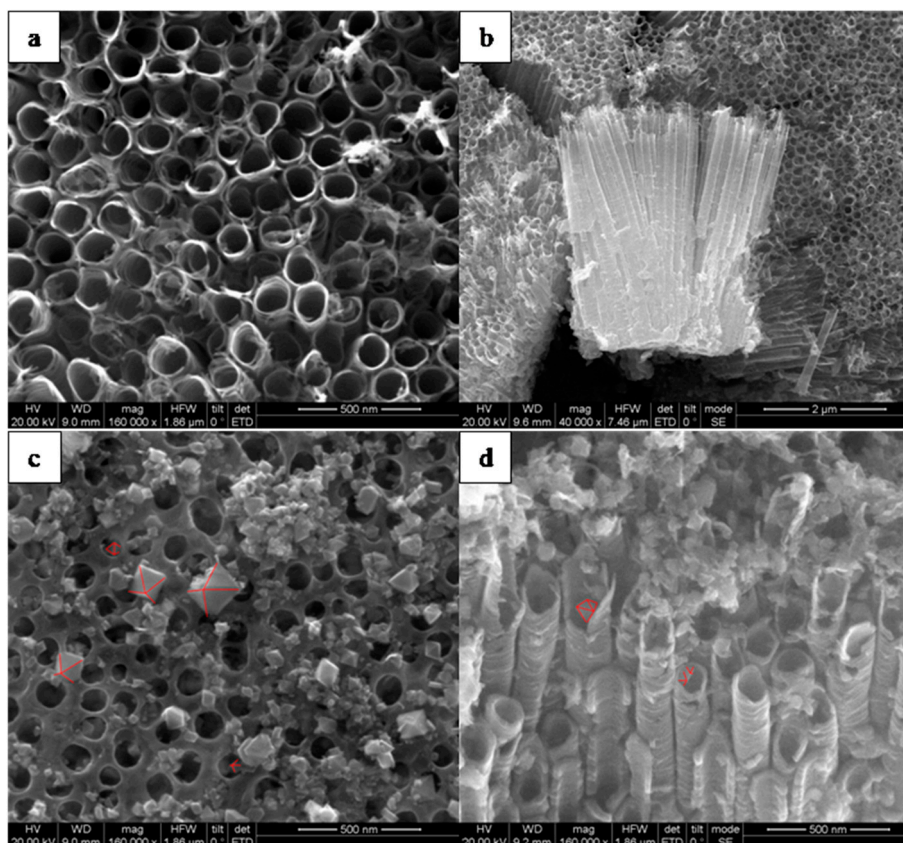


**Figure 2.** (a,b) SEM images of the TiO<sub>2</sub> NTAs and (c,d) SEM images of the as-synthesized CdIn<sub>2</sub>S<sub>4</sub>/TiO<sub>2</sub> NTA composites.

### 2.1.3. XPS Analysis

A total survey spectrum of the synthesized composite is shown in Figure 3a. The peaks of S, In, Cd, O, and Ti elements can be observed from the survey spectrum. The existence of S (II) in the fresh CdIn<sub>2</sub>S<sub>4</sub>/TiO<sub>2</sub> NTA composite is indicated by the closely spaced spin-orbit components ( $\Delta = 1.16$  eV and intensity ratio = 0.511) at approximately 161.3 eV (Figure 3b). Meanwhile, the In (IV) 3d spectrum exhibits two broad peaks, namely, 3d<sub>5/2</sub> and 3d<sub>3/2</sub> (resulting from the spin-orbit splitting) without any loss features in the high binding energy side. The two peaks are located at 444.6 and 452.2 eV (Figure 3c) and can be assigned to CdIn<sub>2</sub>S<sub>4</sub>. For Cd, two broad peaks appear near 405 eV with well-separated spin-orbit components ( $\Delta = 6.8$  eV) on the spectrum. The loss features, which cannot be observed in the high binding energy side of the 3d<sub>3/2</sub> spin-orbit component, indicate that the Cd was trivalent. The O (II) and Ti (IV) in TiO<sub>2</sub> are presented in Figure 3e,f, respectively. Figure 4 indicates the presence of hydroxyl groups on the surface of TiO<sub>2</sub>.

In addition, the valence band of the monomers was determined by two monomer XPS testing. In Figure 3g,h, the straight line near 0 eV in the obtained graph was extrapolated to intersect with the horizontal extension line. The intersection point (1.39 eV) denotes the valence band (E<sub>v</sub>) of the synthetic material, and the E<sub>v</sub> of the synthetic TiO<sub>2</sub> was found to be 2.81 eV.

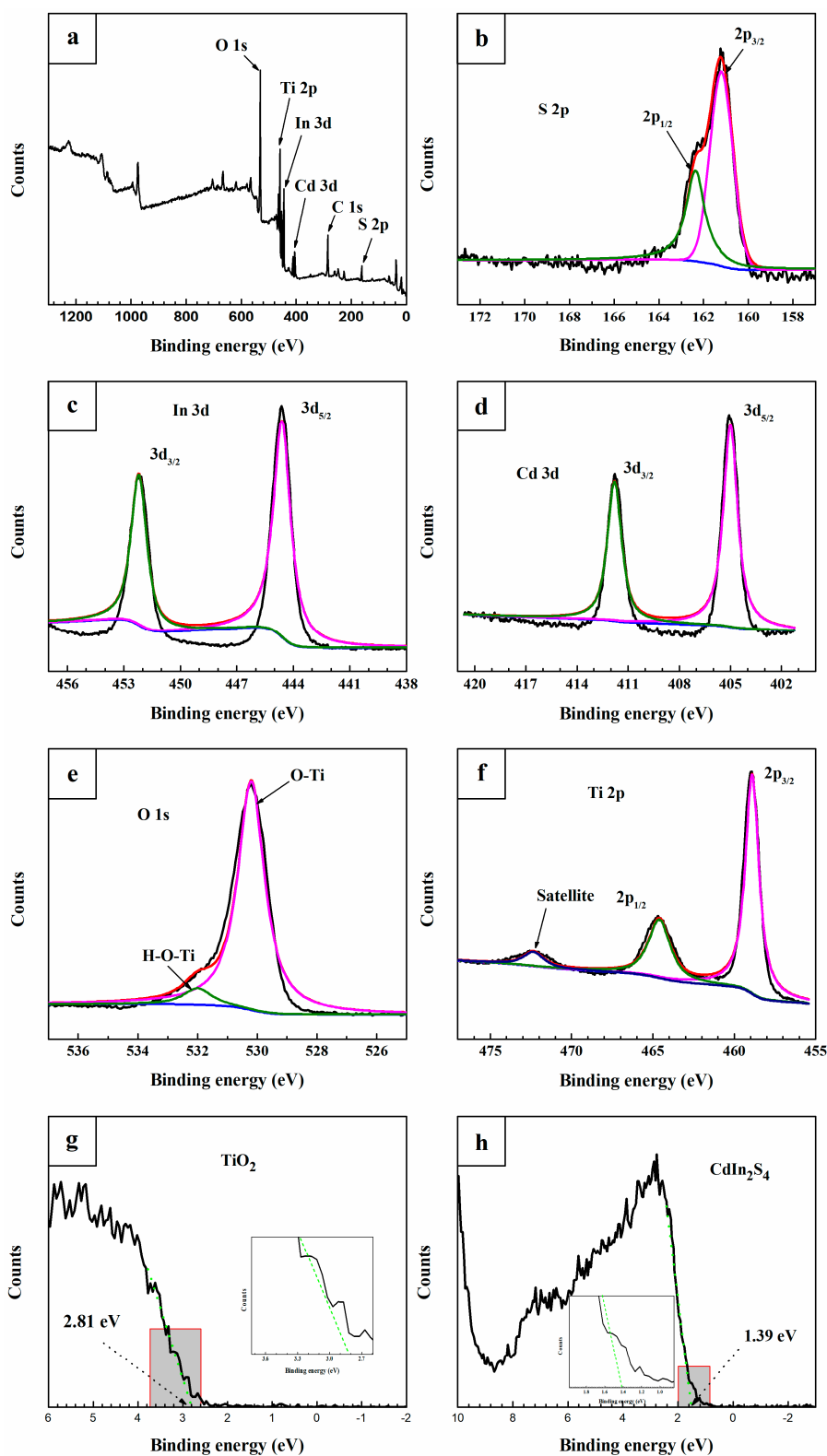


**Figure 3.** (a) X-ray photoelectron spectroscopy (XPS) survey; (b–f) S 2p, In 3d, Cd 3d, O 1s, and Ti 2p on the surface of the synthesized CdIn<sub>2</sub>S<sub>4</sub>/TiO<sub>2</sub> NTA composites; and (g,h) the valence band of the synthesized TiO<sub>2</sub> NTAs and CdIn<sub>2</sub>S<sub>4</sub>.

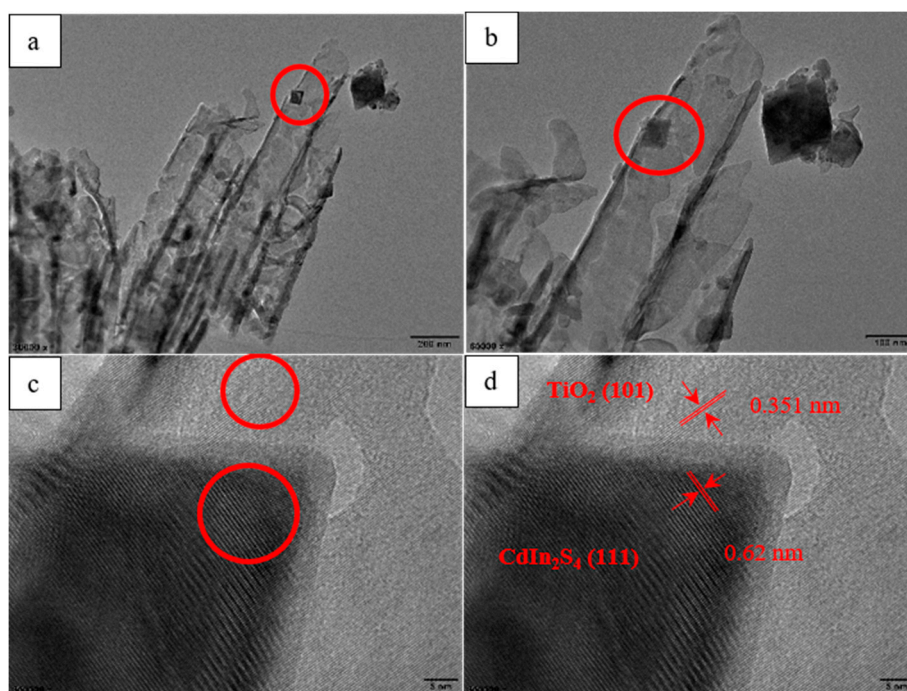


**Figure 4.** TEM (a,b) and HRTEM (c,d) morphologies of the synthesized CdIn<sub>2</sub>S<sub>4</sub>/TiO<sub>2</sub> NTA composites.

#### 2.1.4. TEM and HRTEM Analysis

A typical low-magnification Transmission electron microscopy (TEM) image of the synthesized CdIn<sub>2</sub>S<sub>4</sub>/TiO<sub>2</sub> NTAs is shown in Figure 4a,b. A batch of nanotubes was clearly developed, forming orderly NTAs; some octahedrons existed on the walls of the TiO<sub>2</sub> nanotubes, which agrees with the SEM results. High resolution transmission electron microscopy (HRTEM) was used to characterize the catalysts after the reaction, as shown in Figure 4c,d. The synthesized sample shows the characteristic 0.351 nm spacing of the (101) lattice plane of anatase TiO<sub>2</sub>. Lattice spacings of around 0.62 nm, which correspond to the distances of the (111) plane of CdIn<sub>2</sub>S<sub>4</sub>, were also observed. These findings indicate that the CdIn<sub>2</sub>S<sub>4</sub> nanoparticles were bound to the TiO<sub>2</sub> NTAs.

#### 2.1.5. UV–Vis Diffuse Reflectance Spectra Analysis

As shown in Figure 5a, the TiO<sub>2</sub> NTAs exhibited a high absorption intensity in the ultraviolet region; its absorption band edge was approximately 385 nm, and the corresponding band gap ( $E_g$ ) was 3.22 eV. These characteristics are typical of anatase. Similarly, CdIn<sub>2</sub>S<sub>4</sub> exhibited effective light absorption at wavelengths less than 590 nm, and the  $E_g$  of CdIn<sub>2</sub>S<sub>4</sub> was 2.1 eV. The absorption of the composite material was much better than that of TiO<sub>2</sub>, and the absorption boundary shifted to 492 nm, thereby extending the absorption range of light. The apparent band gap of the corresponding composite material was 2.52 eV. The introduction of CdIn<sub>2</sub>S<sub>4</sub> slightly narrowed the apparent band gap of TiO<sub>2</sub>, thereby allowing the semiconductor to absorb visible light with a large percentage of solar energy.

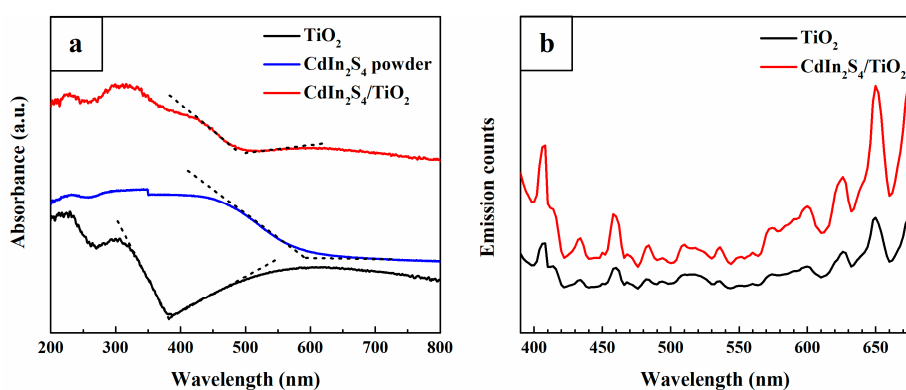


**Figure 5.** (a) UV-VIS diffuse reflectance spectra of the prepared TiO<sub>2</sub> NTAs and CdIn<sub>2</sub>S<sub>4</sub>/TiO<sub>2</sub> NTA composites; (b) photoluminescence (PL) spectra of the synthesized TiO<sub>2</sub> NTAs and CdIn<sub>2</sub>S<sub>4</sub>/TiO<sub>2</sub> NTA composites.

In combination with the valence band position of the composite material, the position of the conduction band ( $E_c$ ) can be calculated using the following formula.

$$E_g = E_v - E_c \quad (1)$$

The  $E_c$  of the synthetic TiO<sub>2</sub> was  $-0.41$  eV, whereas that of the CdIn<sub>2</sub>S<sub>4</sub> was  $-0.71$  eV. These factors indicate that the prepared TiO<sub>2</sub> NTAs and CdIn<sub>2</sub>S<sub>4</sub> were as expected. Moreover, the synthetic composite showed excellent absorption performance of visible light and provided photocathodic protection for Q235.

#### 2.1.6. Photoluminescence (PL) Spectra Analysis

PL spectra of CdIn<sub>2</sub>S<sub>4</sub>/TiO<sub>2</sub> and TiO<sub>2</sub> NTAs at the same excitation wavelength are shown in Figure 5b. The same shapes of the two curves indicate that the supported CdIn<sub>2</sub>S<sub>4</sub> did not increase the recombination of photo-induced electrons and holes within the wavelength range of less than approximately 590 nm. The spectral intensity of the CdIn<sub>2</sub>S<sub>4</sub>/TiO<sub>2</sub> NTAs composite was stronger than that of pure TiO<sub>2</sub> NTAs. This finding that the amount of photo-induced electrons or holes for recombination increased in TiO<sub>2</sub> NTAs is due to the supported CdIn<sub>2</sub>S<sub>4</sub> nanoparticles. This increase is due to the transfer of photo-induced electrons from the conduction band of CdIn<sub>2</sub>S<sub>4</sub> to that of TiO<sub>2</sub>. In the large wavelength range, the spectral intensity increased with different intensifications due to the recombination of photo-induced carriers in CdIn<sub>2</sub>S<sub>4</sub>.

#### 2.1.7. Photochemical Analysis

Photoinduced volt-ampere characteristic curves under intermittent visible light ( $i$ - $V$  curves) [31,32] were used to test the photoelectric chemical properties of the synthesized materials. Figure 6 shows the  $i$ - $V$  curves of the samples. Negative photo-induced potential and positive photo-induced current density indicate that TiO<sub>2</sub> is a typical n-type semiconductor. The photocurrent started to flow at  $-1.4$  V (versus the saturated calomel electrode (SCE)) and the onset potential was negative compared with its Fermi level. This phenomenon was due to the negative shift of the Fermi level of TiO<sub>2</sub> under alkaline conditions [20,33,34]. The  $i$ - $V$  curves of the synthetic CdIn<sub>2</sub>S<sub>4</sub>/TiO<sub>2</sub> NTA composite showed a higher photocurrent density than that of TiO<sub>2</sub>. This finding indicates that any composite other than TiO<sub>2</sub> can easily inject electrons into Q235 in need of protection. In particular, at the corrosion potential of Q235 (from the Tafel curve), the photo-induced electrons were fully capable of transferring from CdIn<sub>2</sub>S<sub>4</sub>/TiO<sub>2</sub> NTAs to Q235 due to the large positive photocurrent. This transfer is beneficial to the photocathodic protection of TiO<sub>2</sub>.

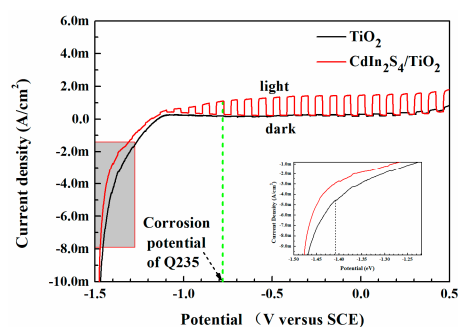


**Figure 6.** Photoinduced volt-ampere characteristic curves under chopped white light illumination of the synthesized TiO<sub>2</sub> NTAs and CdIn<sub>2</sub>S<sub>4</sub>/TiO<sub>2</sub> NTA composites. Legend: SCE, saturated calomel electrode.

Tafel polarization curves of Q235 with and without composite semiconductor materials are shown in Figure 7.

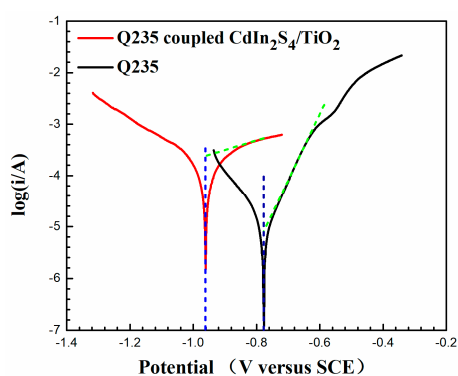


**Figure 7.** Tafel polarization curves of Q235 with and without composite semiconductor materials.

On the curve of pure Q235, the self-corrosion current of pure Q235 was the current value extrapolated from the straight part of the anode area to the self-corrosion potential on the level of  $10^{-6}$  A. The left branch of the polarization curve shows a transient platform, indicating the existence of the cathode reaction of concentration polarization of O<sub>2</sub>. On the curve of Q235 coupled with CdIn<sub>2</sub>S<sub>4</sub>/TiO<sub>2</sub> NTAs, the extrapolation values obtained by the same method in the cathode zone are similar to those obtained by *i*-*V* curves at  $-0.96$  V (the equilibrium potential from the Tafel curve). This finding explains why the polarization curve of Q235 coupled with CdIn<sub>2</sub>S<sub>4</sub>/TiO<sub>2</sub> NTAs was found to be above that without coupled CdIn<sub>2</sub>S<sub>4</sub>/TiO<sub>2</sub>. The equilibrium potential demonstrates a negative shift when Q235 was coupled with the CdIn<sub>2</sub>S<sub>4</sub>/TiO<sub>2</sub> photo-anode due to the existence of the photo-induced electrons. Nonetheless, the dissolving current of Fe decreased under negative potential.

The variations in the potentials of the Q235 electrode coupled with the photo-anode and the current densities from Q235 to the synthetic composite with non-polarization under intermittent visible light were measured to characterize the photocathodic protection performance of the synthetic photo-anode. Figure 8a shows that the potential of Q235 coupled with TiO<sub>2</sub> NTAs continued to decrease and slightly fluctuated when the light was turned on and off. This finding indicates that TiO<sub>2</sub> NTAs have no photocathodic protection effect on Q235 and may even accelerate the corrosion of Q235. For CdIn<sub>2</sub>S<sub>4</sub>/TiO<sub>2</sub> NTAs, the potential drop of Q235 coupled with CdIn<sub>2</sub>S<sub>4</sub>/TiO<sub>2</sub> NTAs reached approximately 400 mV when visible light was switched on. Q235 was therefore polarized to  $-1.0$  V. Ch. Barchiche et al. [35] have proven that Q235 is effectively resistant to corrosion from XRD, SEM, and electrochemical methods. Other studies [36–38] have also shown that Q235 might be effectively resistant to corrosion when polarized to  $-0.9$ – $-1.2$  V. Hence, the polarization of Q235 to  $-1.0$  V could be considered effective protection from corrosion [39–41]. The dissolution of Fe was substantially inhibited in this potential. This inhibition is due to the response of CdIn<sub>2</sub>S<sub>4</sub> to visible light, the n–n

type heterojunctions, and the more negative  $E_c$  of  $\text{CdIn}_2\text{S}_4$  compared with that of  $\text{TiO}_2$ , contributing to the photocathodic protection effect of the composite on Q235. Figure 8b shows that the current density was negative with and without visible light for  $\text{TiO}_2$  NTAs. This result indicates that Q235 was able to accelerate corrosion when coupled with the  $\text{TiO}_2$  NTAs. For the  $\text{CdIn}_2\text{S}_4/\text{TiO}_2$  NTAs, current density sharply increased along the positive direction when the visible light was switched on for the photoelectrode. This finding suggests that a large number of electrons and holes were generated and that the photocurrent was maintained at a relatively stable level. Moreover, the photocurrent density of  $\text{CdIn}_2\text{S}_4/\text{TiO}_2$  NTAs reached approximately  $50 \text{ mA/cm}^2$ , which was larger than the current produced by the reduction of  $\text{O}_2$  and  $\text{H}^+$  (reference self-corrosion current). These findings suggested that Q235 was protected by the coupled photoelectrode under visible light. The high photocurrent can also polarize the coupled Q235 electrode to a much more negative potential, thereby providing an improved cathodic protection. Overall,  $\text{CdIn}_2\text{S}_4/\text{TiO}_2$  NTAs showed an effective photocathodic protection effect on Q235 under visible light.

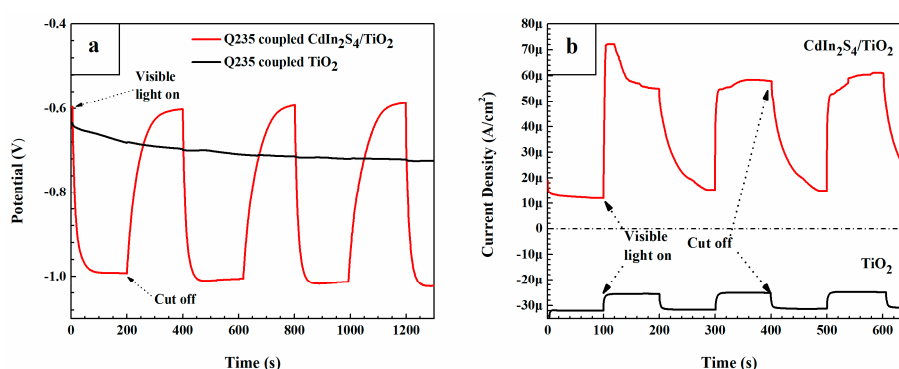


**Figure 8.** (a) Variations of the potentials and (b) current densities of the Q235 electrode coupled with the synthesized  $\text{CdIn}_2\text{S}_4/\text{TiO}_2$  NTA photoelectrodes under intermittent light illumination.

A mechanism describing the enhanced photocathodic protection performance of the synthesized  $\text{CdIn}_2\text{S}_4/\text{TiO}_2$  NTA photoelectrode is illustrated in Figure 9.  $\text{TiO}_2$  and  $\text{In}_2\text{S}_3$  can produce a large number of photo-induced charge carriers under bright visible light exposure. The separation of photo-induced carriers is accelerated by the construction of an n-n heterojunction considering the flow of photo-induced electrons from the conduction band of  $\text{CdIn}_2\text{S}_4$  into the conduction band of  $\text{TiO}_2$ . The holes from  $\text{CdIn}_2\text{S}_4$  and  $\text{TiO}_2$  are then consumed by the hole trapping agent in the solution. Q235 is protected by the transfer of photo-induced electrons from  $\text{TiO}_2$  to Q235 because the dissolution of Fe is inhibited at a relatively negative potential.

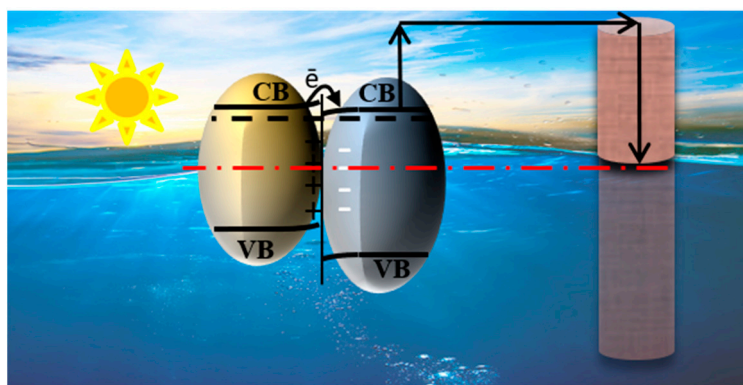


**Figure 9.** A schematic illustration for the fabrication of  $\text{CdIn}_2\text{S}_4/\text{TiO}_2$  NTA composites for photocathodic protection of Q235.

### 3. Experiment

#### 3.1. Materials

All reagents involved in this work were purchased and used directly without any purification.  $\text{NH}_4\text{F}$ , AR was obtained from Shanghai Macklin Biochemical Co., Ltd. (Shanghai, China).  $\text{In}(\text{NO}_3)_3 \cdot 4.5\text{H}_2\text{O}$ ,  $\text{Na}_2\text{S} \cdot 9\text{H}_2\text{O}$ ,  $\text{NaCl}$ ,  $\text{Na}_2\text{SO}_3$ ,  $\text{C}_2\text{H}_5\text{NS}$  (thioacetamide),  $\text{CH}_3\text{CH}_2\text{OH}$  (ethyl alcohol), and  $(\text{CH}_2\text{OH})_2$  (ethylene glycol) were obtained from Sinopharm Chemical Reagent Co., Ltd. (Shanghai, China).  $\text{Cd}(\text{NO}_3)_2 \cdot 4\text{H}_2\text{O}$  was acquired from Shanghai Aladdin Biochemical Technology Co., Ltd. (Shanghai, China). All the above chemicals used in the experiments were of analytical reagent grade. A custom-made H-type photochemical electrolytic cell was obtained from Tianjin Aida Heng Sheng Technology Development Co., Ltd. (Tianjin, China).

#### 3.2. Preparation of $\text{TiO}_2$ NTA and $\text{CdIn}_2\text{S}_4/\text{TiO}_2$ NTA Composites

A two-step anodization process [42,43] was performed to prepare the NTAs using Pt foil, Ti foil, and  $\text{NH}_4\text{F}$  solution as a cathode, an anode, and an electrolyte, respectively, to produce  $\text{TiO}_2$ . The Ti foil (99.99%, 0.30 mm) was cut into  $10 \times 30 \text{ mm}^2$  foil pieces and was ultrasonically washed with deionized water, ethyl ethanol, and acetone 10 min before its usage. The Pt foil was a  $1.0 \times 1.0 \text{ cm}^2$  commercial platinum electrode. The  $\text{NH}_4\text{F}$  solution was obtained by dissolving 1.72 g  $\text{NH}_4\text{F}$  in 50 mL deionized water and mixing well with 450 mL ethylene glycol. The voltage of anodic oxidation was set to 60.0 V. After the first step of anodizing, the Ti foil was placed in 1 M of HCl for ultrasonic cleaning until a glossy surface was realized. The conditions for the second oxidation were exactly the same as those for the first oxidation. The oxidized Ti sheet was rinsed with deionized water to remove the electrolyte solution from the surface and air dried afterward. The oxidized Ti foil was then placed in the muffle furnace, calcined at  $450 \text{ }^\circ\text{C}$  for 120 min, and left to cool at room temperature. The  $\text{TiO}_2$  NTAs were successfully prepared on the surface of the Ti foil.

A facile hydrothermal method was used to load  $\text{CdIn}_2\text{S}_4$  nanoparticles onto the surface of the  $\text{TiO}_2$  NTAs. In this synthesis, 0.4 mmol of  $\text{Cd}(\text{NO}_3)_2 \cdot 4\text{H}_2\text{O}$ , 0.8 mmol of  $\text{In}(\text{NO}_3)_3 \cdot 4.5\text{H}_2\text{O}$ , and 3.2 mmol of  $\text{C}_2\text{H}_5\text{NS}$  were dissolved in an ethanol solution containing 15.0 mL of deionized water and 15.0 mL of ethanol. After stirring for 20 min, the mixed solution and prepared  $\text{TiO}_2$  NTAs were transferred to a 100 mL Teflon-lined autoclave and heated at  $180 \text{ }^\circ\text{C}$  for 24 h. After the hydrothermal reaction, the Ti foil was rinsed with absolute ethanol and deionized water several times and dried at  $80 \text{ }^\circ\text{C}$  for 12 h. A  $\text{CdIn}_2\text{S}_4/\text{TiO}_2$  NTA composite was eventually synthesized.

XRD patterns were used to detect the crystalline structures of the synthesized  $\text{CdIn}_2\text{S}_4/\text{TiO}_2$  NTAs and monomers using a Bruker D8 Advance diffractometer with  $\text{Cu K}\alpha$  radiation ( $\lambda = 0.154 \text{ nm}$ ). The monomer of  $\text{CdIn}_2\text{S}_4$  was collected from the bottom of the Teflon-lined autoclave and dried at  $80 \text{ }^\circ\text{C}$  after washing in deionized water and absolute ethanol successively. The surface morphology of the samples was observed on a Hitachi S-4800 field-emission SEM, and the section was obtained by warping the edges caused by cutting. The surface chemical composition and chemical state of the samples were analyzed using XPS (ESCALAB 250XI, Thermo Fisher Scientific, Waltham, US) with  $\text{Al K}\alpha$  ( $h\nu = 1486.6 \text{ eV}$ ). TEM (JEM-F200, JEOL, Tokyo, Japan) was employed to characterize the microstructure of the  $\text{CdIn}_2\text{S}_4/\text{TiO}_2$  NTAs. The UV-VIS diffuse reflectance (HITACHI U-3900H, HITACHI, Tokyo, Japan) and  $\text{TiO}_2$  photoluminescence spectra (Edinburgh FLS980) were measured to explore the optical effect of loading  $\text{CdIn}_2\text{S}_4$ . Photoluminescence spectra were used to characterize the recombination rates of photo-induced carriers using a FLS980 Series fluorescence spectrometer (UK).

#### 3.3. Electrochemical Measurements

Each electrode had an exposed area of  $1.0 \times 1.0 \text{ cm}^2$ . The Q235 electrodes were sanded with 600, 800, 1000, 2000, and 3000 mesh sandpapers successively before being used.

The photo-induced volt-ampere characteristic curves were realized in a three-electrode configuration in a 0.35 M  $\text{Na}_2\text{SO}_3$  and 0.25 M  $\text{Na}_2\text{S}$  solution. The synthesized materials, SCE,

and Pt electrode were used as the working, reference, and counter electrodes, respectively. The *i*-*V* curves were measured from  $-1.5$  V to  $0.5$  V with a scan rate of  $0.02$  V/s and with visible light switched on and off every 2 s. The working, reference, and counter electrodes were the Q235 electrode, SCE, and Pt electrode, respectively.

Tafel plots, variations in the potentials, and the current densities under intermittent visible light were achieved in an H-type electrolytic cell. This cell was divided into the photocell and the corrosion cell was connected by a Nafion membrane. The electrolyte in the photocell was  $0.35$  M  $\text{Na}_2\text{SO}_3$  and was placed in a  $0.25$  M  $\text{Na}_2\text{S}$  solution. The synthesized materials connected by a copper wire were placed in this cell. Meanwhile, the SCE, Pt electrode, and Q235 electrode were placed in the corrosion cell with a  $3.5$  wt.% NaCl solution. The Tafel plots for Q235 were obtained at a voltage range of  $-300$  mV to  $300$  mV considering the open circuit at a scan rate of  $0.166$  mV/s, and Q235 was coupled with the synthesized materials under visible light.

The effect of photocathodic protection was determined by variations in the potential and current density tests. A Xe lamp and  $3.5$  wt.% NaCl solution were used to simulate intense solar light and seawater respectively. These properties were realized in an H-type electrolytic cell. In the variations in the potential test, Q235 coupled with the synthesized materials, SCE, and Pt electrode were used as the working, reference, and counter electrodes, respectively. The synthesized materials were irradiated with visible light every 200 s for 200 s at a time. In the current density test, Q235 was connected to the ground wire (GND wire), the synthesized materials were connected to the working electrode, and the counter and reference electrode wires were short connected. The synthesized materials were irradiated with visible light every 100 s for 100 s at a time.

#### 4. Conclusions

In this work,  $\text{CdIn}_2\text{S}_4/\text{TiO}_2$  NTA nanocomposites were successfully prepared via two-step anodization of Ti followed by a hydrothermal method. The  $\text{CdIn}_2\text{S}_4$  nanoparticles were distributed on the top surface of the NTAs and the tube walls with a relatively symmetrical octahedral structure. The optical absorption region was expanded and optical absorption in the visible light region was enhanced relative to  $\text{TiO}_2$  NTAs, thereby facilitating the utilization of visible light. The PL curves indicate that the enhanced photocathodic protection of  $\text{CdIn}_2\text{S}_4/\text{TiO}_2$  NTA nanocomposites can be ascribed to the formation of an effective n-n type heterojunction electronic field at the interface of  $\text{CdIn}_2\text{S}_4$  and  $\text{TiO}_2$ . This electronic field remarkably improves the separation efficiency of the photo-induced electron-hole pairs. The feasibility of converting excellent optical properties to electrical properties was examined by *i*-*V* and Tafel curves. The results of the variations in the potentials and the current densities indicates that  $\text{CdIn}_2\text{S}_4/\text{TiO}_2$  nanocomposites can provide a favorable photoelectrochemical cathodic protection for the coupled Q235 under visible light in the simulated splash zone.

**Author Contributions:** All authors have read and agree to the published version of the manuscript. Conceptualization, Z.M. and X.M.; methodology, Z.M. and X.L.; validation, X.M., X.W. and N.L.; investigation, Z.M.; resources, B.H.; data curation, X.M.; writing—original draft preparation, Z.M.; writing—review and editing, Z.M., N.L. and X.W.; supervision, B.H.; project administration, B.H.; funding acquisition, B.H.

**Funding:** The Chinese Academy of Engineering (no. 2017-XZ-16); the National Natural Science Foundation of China (no. 41827805); the Chinese Academy of Engineering (no. 2019-XZ-21).

**Conflicts of Interest:** The authors declare no conflict of interest.

#### References

1. Qian, B.; Hou, B.; Zheng, M. The inhibition effect of tannic acid on mild steel corrosion in seawater wet/dry cyclic conditions. *Corros. Sci.* **2013**, *72*, 1–9. [[CrossRef](#)]
2. Liu, F.G.; Du, M.; Zhang, J.; Qiu, M. Electrochemical behavior of Q235 steel in saltwater saturated with carbon dioxide based on new imidazoline derivative inhibitor. *Corros. Sci.* **2009**, *51*, 102–109. [[CrossRef](#)]

3. Qu, D.R.; Zheng, Y.G.; Jing, H.M.; Yao, Z.M.; Ke, W. High temperature naphthenic acid corrosion and sulphidic corrosion of Q235 and 5Cr1/2Mo steels in synthetic refining media. *Corros. Sci.* **2006**, *48*, 1960–1985. [[CrossRef](#)]
4. Wang, B.; Du, M.; Zhang, J.; Gao, C.J. Electrochemical and surface analysis studies on corrosion inhibition of Q235 steel by imidazoline derivative against CO<sub>2</sub> corrosion. *Corros. Sci.* **2011**, *53*, 353–361. [[CrossRef](#)]
5. Al-Fozan, S.A.; Malik, A.U. Effect of seawater level on corrosion behavior of different alloys. *Desalination* **2008**, *228*, 61–67. [[CrossRef](#)]
6. Balabanić, G.; Bićanić, N.; Dureković, A. Mathematical Modeling of Electrochemical Steel Corrosion in Concrete. *J. Eng. Mech.* **1996**, *122*, 1113–1122. [[CrossRef](#)]
7. Melchers, R.E. Probabilistic Model for Marine Corrosion of Steel for Structural Reliability Assessment. *J. Struct. Eng.* **2003**, *129*, 1484–1493. [[CrossRef](#)]
8. Zen, K. Corrosion and life cycle management of port structures. *Corros. Sci.* **2005**, *47*, 2353–2360. [[CrossRef](#)]
9. Zhao, W.-M.; Wang, Y.; Liu, C.; Dong, L.-X.; Yu, H.-H.; Ai, H. Erosion–corrosion of thermally sprayed coatings in simulated splash zone. *Surf. Coat. Technol.* **2010**, *205*, 2267–2272. [[CrossRef](#)]
10. Breslin, C.B.; Macdonald, D.D.; Sikora, E.; Sikora, J. Photo-inhibition of pitting corrosion on types 304 and 316 stainless steels in chloride-containing solutions. *Electrochim. Acta* **1997**, *42*, 137–144. [[CrossRef](#)]
11. Moussa, S.O.; Hocking, M.G. The photo-inhibition of localized corrosion of 304 stainless steel in sodium chloride environment. *Corros. Sci.* **2001**, *43*, 2037–2047. [[CrossRef](#)]
12. Song, L.; Chen, Z. The role of UV illumination on the NaCl-induced atmospheric corrosion of Q235 carbon steel. *Corros. Sci.* **2014**, *86*, 318–325. [[CrossRef](#)]
13. Fujisawa, R.; Tsujikawa, S. Photo-Protection of 304 Stainless Steel with TiO<sub>2</sub> Coating. *Mater. Sci. Forum* **1995**, *185–188*, 1075. [[CrossRef](#)]
14. Ohko, Y.; Saitoh, S.; Tatsuma, T.; Fujishima, A. Photoelectrochemical Anticorrosion and Self-Cleaning Effects of a TiO<sub>2</sub> Coating for Type 304 Stainless Steel. *J. Electrochem. Soc.* **2001**, *148*. [[CrossRef](#)]
15. Yuan, J.; Tsujikawa, S. Photo-Effects of Sol-Gel Derived TiO<sub>2</sub> Coating on Carbon Steel in Alkaline Solution. *Zairyo-to-Kankyo* **1995**, *44*, 534–542. [[CrossRef](#)]
16. Jing, J.; Sun, M.; Chen, Z.; Li, J.; Xu, F.; Xu, L. Enhanced Photoelectrochemical Cathodic Protection Performance of the Secondary Reduced Graphene Oxide Modified Graphitic Carbon Nitride. *J. Electrochem. Soc.* **2017**, *164*, C822–C830. [[CrossRef](#)]
17. Li, X.; Wang, X.; Ning, X.; Lei, J.; Shao, J.; Wang, W.; Huang, Y.; Hou, B. Sb<sub>2</sub>S<sub>3</sub>/Sb<sub>2</sub>O<sub>3</sub> modified TiO<sub>2</sub> photoanode for photocathodic protection of 304 stainless steel under visible light. *Appl. Surf. Sci.* **2018**, *462*, 155–163. [[CrossRef](#)]
18. Wang, X.T.; Ning, X.B.; Shao, Q.; Ge, S.S.; Fei, Z.Y.; Lei, J.; Hou, B.R. ZnFeAl-layered double hydroxides/TiO<sub>2</sub> composites as photoanodes for photocathodic protection of 304 stainless steel. *Sci. Rep.* **2018**, *8*, 4116. [[CrossRef](#)]
19. Chen, X.; Shen, S.; Guo, L.; Mao, S.S. Semiconductor-based photocatalytic hydrogen generation. *Chem. Rev.* **2010**, *110*, 6503–6570. [[CrossRef](#)]
20. Fujishima, A.; Zhang, X.; Tryk, D. TiO<sub>2</sub> photocatalysis and related surface phenomena. *Surf. Sci. Rep.* **2008**, *63*, 515–582. [[CrossRef](#)]
21. Linsebigler, A.L.; Lu, G.; Yates, J.T. Photocatalysis on TiO<sub>2</sub> Surfaces: Principles, Mechanisms, and Selected Results. *Chem. Rev.* **1995**, *95*, 735–758. [[CrossRef](#)]
22. Zhang, X.; Su, X.; Gao, W.; Wang, F.; Liu, Z.; Zhan, J.; Liu, B.; Wang, R.; Liu, H.; Sang, Y. Photocatalytic quartz fiber felts with carbon-connected TiO<sub>2</sub> nanoparticles for capillarity-driven continuous-flow water treatment. *Appl. Phys. A* **2018**, *124*. [[CrossRef](#)]
23. Zhang, X.; Wang, Y.; Liu, B.; Sang, Y.; Liu, H. Heterostructures construction on TiO<sub>2</sub> nanobelts: A powerful tool for building high-performance photocatalysts. *Appl. Catal. B Environ.* **2017**, *202*, 620–641. [[CrossRef](#)]
24. Guillot-Deudon, C.; Caldes, M.T.; Stolaroff, A.; Choubrac, L.; Paris, M.; Latouche, C.; Barreau, N.; Lafond, A.; Jobic, S. Crystal Chemistry, Optical-Electronic Properties, and Electronic Structure of Cd<sub>1-x</sub>In<sub>2+2x</sub>/3S<sub>4</sub> Compounds (0 ≤ x ≤ 1), Potential Buffer in CIGS-Based Thin-Film Solar Cells. *Inorg. Chem.* **2018**, *57*, 12624–12631. [[CrossRef](#)]
25. Jiang, Y.; Peng, Z.; Wu, F.; Xiao, Y.; Jing, X.; Wang, L.; Liu, Z.; Zhang, J.; Liu, Y.; Ni, L. A novel 3D/2D CdIn<sub>2</sub>S<sub>4</sub> nano-octahedron/ZnO nanosheet heterostructure: Facile synthesis, synergistic effect and enhanced tetracycline hydrochloride photodegradation mechanism. *Dalton Trans* **2018**, *47*, 8724–8737. [[CrossRef](#)]

26. Liu, Y.; Li, L.; Wang, R.; Li, J.; Huang, J.; Zhang, W. Multi-mode photocatalytic performances of CdS QDs modified CdIn<sub>2</sub>S<sub>4</sub>/CdWO<sub>4</sub> nanocomposites with high electron transfer ability. *J. Nanopart. Res.* **2018**, *20*, 319. [[CrossRef](#)]
27. Mahadadalkar, M.A.; Gosavi, S.W.; Kale, B.B. Interstitial charge transfer pathways in a TiO<sub>2</sub>/CdIn<sub>2</sub>S<sub>4</sub> heterojunction photocatalyst for direct conversion of sunlight into fuel. *J. Mater. Chem. A* **2018**, *6*, 16064–16073. [[CrossRef](#)]
28. Thakur, P.; Chadha, R.; Biswas, N.; Sarkar, S.K.; Mukherjee, T.; Joshi, S.S.; Kapoor, S. Synthesis and characterization of CdS doped TiO<sub>2</sub> nanocrystalline powder: A spectroscopic study. *Mater. Res. Bull.* **2012**, *47*, 1719–1724. [[CrossRef](#)]
29. Ye, X.; Chen, Y.; Ling, C.; Zhang, J.; Meng, S.; Fu, X.; Wang, X.; Chen, S. Chalcogenide photocatalysts for selective oxidation of aromatic alcohols to aldehydes using O<sub>2</sub> and visible light: A case study of CdIn<sub>2</sub>S<sub>4</sub>, CdS and In<sub>2</sub>S<sub>3</sub>. *Chem. Eng. J.* **2018**, *348*, 966–977. [[CrossRef](#)]
30. Song, J.P.; Yin, P.F.; Mao, J.; Qiao, S.Z.; Du, X.W. Catalytically active and chemically inert CdIn<sub>2</sub>S<sub>4</sub> coating on a CdS photoanode for efficient and stable water splitting. *Nanoscale* **2017**, *9*, 6296–6301. [[CrossRef](#)]
31. Sakai, N.; Ebina, Y.; Takada, K.; Sasaki, T. Electronic band structure of titania semiconductor nanosheets revealed by electrochemical and photoelectrochemical studies. *J. Am. Chem. Soc.* **2004**, *126*, 5851–5858. [[CrossRef](#)] [[PubMed](#)]
32. Alpuche-Aviles, M.A.; Wu, Y. Photoelectrochemical study of the band structure of Zn<sub>2</sub>SnO<sub>4</sub> prepared by the hydrothermal method. *J. Am. Chem. Soc.* **2009**, *131*, 3216–3224. [[CrossRef](#)] [[PubMed](#)]
33. Chen, F.; Li, X.; Hihath, J.; Huang, Z.; Tao, N. Effect of anchoring groups on single-molecule conductance: Comparative study of thiol-, amine-, and carboxylic-acid-terminated molecules. *J. Am. Chem. Soc.* **2006**, *128*, 15874–15881. [[CrossRef](#)] [[PubMed](#)]
34. Chun, W.-J.; Ishikawa, A.; Fujisawa, H.; Takata, T.; Kondo, J.N.; Hara, M.; Kawai, M.; Matsumoto, Y.; Domen, K. Conduction and Valence Band Positions of Ta<sub>2</sub>O<sub>5</sub>, TaON, and Ta<sub>3</sub>N<sub>5</sub> by UPS and Electrochemical Methods. *J. Phys. Chem. B* **2003**, *107*, 1798–1803. [[CrossRef](#)]
35. Barchiche, C.; Deslouis, C.; Festy, D.; Gil, O.; Refait, P.; Touzain, S.; Tribollet, B. Characterization of calcareous deposits in artificial seawater by impedance techniques 3—Deposit of CaCO<sub>3</sub> in the presence of Mg(II). *Electrochim. Acta* **2003**, *48*, 1645–1654. [[CrossRef](#)]
36. Rendón Belmonte, M.; Trinidad Pérez Quiroz, J.; Valdez Salas, B.; Martínez Madrid, M.; Torres Acosta, A.; Porcayo Calderón, J.; Schorr Wiener, M. Characterization of steel surface under cathodic protection in seawater. *Anti-Corros. Methods Mater.* **2013**, *60*, 160–167. [[CrossRef](#)]
37. Tsuru, T.; Dae-Hi, J.; Haruyama, S. Impedance Characteristics of the Metals under Cathodic Protection and Determination of an Optimum Protection Potential. *Corros. Eng.* **1985**, *34*, 36–41. [[CrossRef](#)]
38. Elbeik, S.; Tseung, A.C.C.; Mackay, A.L. The formation of calcareous deposits during the corrosion of mild steel in sea water. *Corros. Sci.* **1986**, *26*, 669–680. [[CrossRef](#)]
39. Li, H.; Li, Y.; Wang, M.; Niu, Z.; Wang, X.; Hou, B. Preparation and photocathodic protection property of ZnIn<sub>2</sub>S<sub>4</sub>/RGO/TiO<sub>2</sub> composites for Q235 carbon steel under visible light. *Nanotechnology* **2018**, *29*, 435706. [[CrossRef](#)]
40. Li, H.; Li, Y.H.; Wang, X.T.; Hou, B.R. 3D ZnIn<sub>2</sub>S<sub>4</sub> nanosheets/TiO<sub>2</sub> nanotubes as photoanodes for photocathodic protection of Q235 CS with high efficiency under visible light. *J. Alloys Compd.* **2019**, *771*, 892–899. [[CrossRef](#)]
41. Ren, J.; Qian, B.; Li, J.; Song, Z.; Hao, L.; Shi, J. Highly efficient polypyrrole sensitized TiO<sub>2</sub> nanotube films for photocathodic protection of Q235 carbon steel. *Corros. Sci.* **2016**, *111*, 596–601. [[CrossRef](#)]
42. Wang, D.; Liu, L. Continuous Fabrication of Free-Standing TiO<sub>2</sub> Nanotube Array Membranes with Controllable Morphology for Depositing Interdigitated Heterojunctions. *Chem. Mater.* **2010**, *22*, 6656–6664. [[CrossRef](#)]
43. Wang, D.; Liu, Y.; Yu, B.; Zhou, F.; Liu, W. TiO<sub>2</sub> Nanotubes with Tunable Morphology, Diameter, and Length: Synthesis and Photo-Electrical/Catalytic Performance. *Chem. Mater.* **2009**, *21*, 1198–1206. [[CrossRef](#)]

